IS-PORTO 2023 PROCEEDINGS

Proceedings of the 8th International Symposium on DEFORMATION CHARACTERISTICS OF GEOMATERIALS Porto, 3rd - 6th September 2023

Anisotropy and cyclic loading characteristics of a stiff Bolders Bank glacial till at Cowden

Tingfa Liu[1#], *Emil* Ushev[2], and *Richard J.* Jardine[3]

[1]*University of Bristol, Department of Civil Engineering, Bristol, United Kingdom*
[2]*ARUP, London, United Kingdom*
[3]*Imperial College London, Department of Civil and Environmental Engineering, London, United Kingdom*
[#] *Corresponding author: tingfa.liu@bristol.ac.uk*

ABSTRACT

Glacial tills are widespread across the world, common in northern Europe and found under the North and Baltic Seas. Their geological and geotechnical characterisation is important to the geotechnical design of a wide range of onshore and offshore structures. This paper reports outcomes from coordinated monotonic small-strain stress probing, cyclic and larger strain triaxial and hollow cylinder apparatus (HCA) testing on a natural low-to-medium plasticity, apparent highly over consolidated, stiff glacial clay till. Monotonic HCA and triaxial experiments investigated the till's stiffness and shear strength anisotropy from its limited linear elastic range up to ultimate failure, showing that stiffnesses are higher in the horizontal direction than in the vertical and that higher undrained shear strengths develop under "passive" horizontal loading than "active" vertical loading. The cyclic triaxial tests revealed the impact of cycling on effective stress paths and strain development, and cyclic stiffness degradation. Stable, metastable and unstable patterns of behaviour are identified, along with different cyclic failure modes, which are related to the till's static yielding behaviour. The experiment results provide the basis for developing, testing and calibrating monotonic and cyclic constitutive models and establishing simplified design procedures for piles installed in comparable tills to support offshore energy and other structures.

Keywords: glacial soils; laboratory tests; anisotropy; cyclic loading.

1. Introduction

Apparently highly overconsolidated stiff glacial clay tills are distributed widely over northern parts of the UK (Davies et al. 2011), northern Europe (Clarke et al. 2008; Clarke 2018) and North America (Fullerton et al. 2003), as well as parts of northern and central Asia, and under the Baltic, North, Norwegian and other Seas. Their geological and geotechnical characterisation is important to a wide range of onshore and offshore engineering design problems that usually involve multi-directional, monotonic and cyclic loading.

The deposition and post-depositional histories of glacial tills can induce anisotropy in their mechanical behaviour, affecting their initial linear elastic stiffness properties through to their yielding and shear strength characteristics. These features can play key roles in the engineering assessment of deformations developed under field loading, soil-structure interaction and ultimate geotechnical stability. Zdravkovic et al. (2001) show how analyses of offshore foundations in soft clays can be improved by considering the anisotropy identified by advanced laboratory testing. Examples involving stiff, overconsolidated UK marine clays include studies by Addenbrooke et al. (1997), Gasparre et al. (2007), Nishimura et al. (2007), Brosse et al. (2016) and Brosse et al. (2017). Other cases include Nishimura's (2014) research on six Japanese sedimentary clays and Ratananikom et al. (2013)'s experiments on lightly over-consolidated Bangkok clay. However, the key experimental evidence required to inform such analyses were lacking for high yield stress ratio (YSR), stiff glacial tills. Understanding their anisotropy will be especially valuable in applications where existing methods perform poorly against field measurements, as in lateral loading analyses of offshore piles (Byrne et al. 2017; Jeanjean et al. 2017) as well as slopes, earthworks, deep excavations, tunnelling and other foundations.

Glacial tills' response to cyclic loading can be particularly important in offshore foundation design, see examples by Andersen (2009) or Jardine et al. (2012). Stress-path laboratory tests on site-specific, or regionally typical, soil types offer an element-level approach for studying how regular cycling influences soil behaviour. Multiple testing programmes involving wide ranges of cyclic conditions have been reported for sands (see for example Wichtmann et al. (2005)) and low-to-medium *OCR* clay sediments (see for example Andersen (2015)). The soil's response is tracked as cycling progresses in terms of permanent strain development, cyclic stiffness and damping ratio changes and, if undrained, mean effective stress or pore pressure drifts; the number of cycles at which any cyclic failure develops is also a key outcome. Significant development has been reported in interpretive constitutive frameworks of varying complexity to simulate cyclic laboratory tests and model boundary value problems. However, these studies focus principally on characterising and modelling the generally contractive cyclic responses of low-to-medium *OCR*, potentially sensitive or structured, clays, little attention has been given to investigating and modelling insensitive, high *OCR* clay tills.

This paper reports coordinated monotonic small-strain stress probing, cyclic and larger strain triaxial and hollow cylinder apparatus (HCA) testing that investigated the mechanical anisotropy and undrained cyclic loading behaviour of stiff, high Yield Stress Ratio (*YSR*, or apparent *OCR*) glacial clay till from the Bolders Bank Formation. The samples were taken from Cowden, on the Holderness peninsula near Hull in NE England where static and cyclic piling research has been conducted since the 1970s. Cowden was also one of the test sites selected for the recent PISA and PICASSO monopile wind-turbine research projects described by Byrne et al. (2017), Zdravković et al. (2020) and Byrne (2021). The laboratory programmes were undertaken as part of Ushev (2018) and Liu (2018)'s doctoral research at Imperial College London and were reported in detail by Liu et al. (2020), Ushev and Jardine (2022a, 2022b). Ushev et al. (2023) establish a comprehensive database of the Cowden glacial till's engineering properties, integrating outcomes from the historical and recent in-situ and laboratory soil characterisation campaigns.

2. Ground conditions and Index properties

Powell & Butcher (2003) and Zdravković et al. (2020a) set out general aspects of the Cowden site ground conditions. The site comprises predominantly, low plasticity glacial clay till to around 12 m depth, below which lies a silty sand layer, then deeper till and chalk. Ushev (2018) confirmed a transition at 4.8 m between red/brown upper weathered till and lower, darker grey-brown, un-weathered layers and reports on how weathering affects index and mechanical properties. While the phreatic surface was located at 1.0 m depth, the profile is under-drained between 5 and 12 m. Table 1 summarises the ranges of index properties over the depth range of interest.

Intact till specimens were prepared from either nominally 100 mm outer diameter cores taken with a triple-barrel, wireline, Geobore-S system down to around 13 m, or high-quality block samples taken in the top 3.5 m of strata. The overall rotary coring recovery rate (42%) was affected by the till's hard gravel inclusions; layers presenting more than 10% gravel could not be recovered satisfactorily. Fig. 1 presents the grading curves of rotary cored intact Cowden till specimens from five depths. The stony till showed on average 7% gravel content and a combined silt and clay faction ranges from 58 to 73% over the considered depth.

Liu (2018) and Liu et al. (2020) categorised the rotary cored and block Cowden samples into four groups according to the degree to which they could be cored in the field or formed into triaxial or HCA test specimens in the laboratory. The key controlling feature was the samples' percentage, by mass, of gravel particles exceeding 2 mm size. Large triaxial specimens (100 mm diameter and 200 mm height) could be formed from the rotary cored samples with typically 7% gravel contents, while the formation of Hollow Cylinder Apparatus (HCA) specimens (typically 180-195 mm height, 71 mm outside and 38 mm inside diameters) was only successful from samples with gravel contents falling below 4%. The HCA programme therefore (unintentionally) considered generally lower-than-typical gravel samples, resulting in systematic, yet not unduly overwhelming, biases regarding shear strengths and stiffnesses.

Table 1. Overview of natural Cowden till index properties

Depth **(m)**	***wc*** **(%)**	***PL*** **(%)**	***LL*** **(%)**	G_s	ρ_{bulk} [g/cm^3]
1.5-2.5	18.0	17.6	38.2	2.723	2.17
2.5-3.5	16.1	17.4	36.4	2.716	2.21
4.0-6.0	16.9	15.1	33.2	2.707	2.19
10-12	17.4	15.5	34.5	2.708	2.18

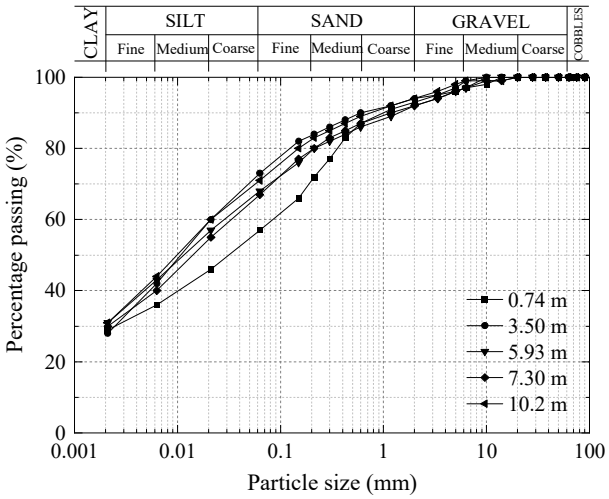

Figure 1. Grading curves of intact rotary cored Cowden till specimens from five depths.

3. Test equipment, procedures and programmes

The monotonic and cyclic triaxial experiments were performed with modified Bishop & Wesley cells on both '38-mm' and '100-mm' diameter specimens. The '100-mm' triaxial systems were also employed in the small-strain probing tests and were configurated with: (a) three 'floating' type LVDT local axial strain sensors spaced 120˚ apart and gauged over the specimen's central 70 mm portion; (b) three 'fixed' LVDTs to measure local radial deformations from three radially spaced points around the specimen's middle height section through a hinged L-shape system. Liu et al. (2022) provided further details of the equipment's resolutions and precisions in stress and strain measurements. A mid-height sensor was employed to track local pore water pressure generation and dissipation in the central zone; three pairs of platen-mounted or lateral 'T-configuration' piezoceramic bender element shear-wave transducers were also installed. Lubricated top and base sample ends consisting of double latex membranes and a thin layer of silicone grease were employed to alleviate platen friction.

The HCA tests were performed with the Imperial College Resonant Column Hollow Cylinder Apparatus (ICRCHCA). The system is equipped with a Hardin oscillator to monitor shear stiffness ($G_{z\theta}$) and damping ratio non-destructively, independently of the consolidation or loading conditions. HCA specimen deformations were gauged globally by a cantilevered axial displacement transducer, two volume-gauges, and

platen-to-platen torsional rotations were sensed through non-contacting proximity transducers, measuring against a shaped cam fixed to the specimen top. System compliance errors were reduced or eliminated through careful calibration. The HCA system provided nominal resolutions and precision ranges of (1-4)×10^{-4}% for all the global strain components.

Liu (2018) and Ushev (2018) highlighted the challenges in preparing high-quality triaxial and HCA specimens from the cored and block samples primarily due to the presence of erratic hard gravel particles, fissures and micro-cracks. They outlined the sample preparation procedures, as well as additional measures and perseverance required to alleviate disturbance and enhance successful rate.

Table 2 summarises the triaxial small-strain probing tests' initial conditions, noting the different K_o (=$\sigma_{h0}'/\sigma_{v0}'$) conditions applied for the specimens from upper (2 to 5.35 m) and deeper horizons. The probing comprised small (typically 2 kPa) drained vertical (dv′), horizontal (dh′) and undrained vertical (dq) stress increments at rates of 0.1-0.2 kPa/hour. Each suite of probing tests on single specimens took 2-2.5 months to complete, while the standard triaxial compression and extension tests typically extended for three weeks.

Table 2. Summary of the triaxial small-strain test conditions

Depth (m)	Test name	Test type†	e_o*	σ_{v0}' (kPa)	σ_{h0}' (kPa)
2.0	PB1	BE, dv′(2), dh′(2), dq(1)	0.461	33.0	49.5
5.1	PB2	BE, dv′(3), dh′(3), dq(1)	0.436	69.9	104.9
12.0	PB3	BE, dv′(2), dh′(2), dq(1)	0.421	223.8	223.8
12.5	PB4	BE, dv′(2), dh′(2), dq(1)	0.406	212.3	218.0

† The numbers enclosed by the brackets denote the number of probes performed. * signifies void ratio after consolidation and creep stages and prior to probing.

The Cowden till's shear strength and stiffness anisotropy were examined through a suite of undrained HCA $\alpha_{d\sigma}$-controlled and simple shear (SS) tests on specimens primarily from a single depth of 2.9 m. As summarised in Table 3, the ultimate failure states were controlled to keep the intermediate principal stress parameter (b) close to 0.5, while covering a range of final α_f values between 0 to 90°. Two undrained triaxial compression (HCA TXC) tests were also performed. HCA simple shear (HCASS) tests were performed by keeping the radial and circumferential strains (ε_r and ε_θ) close to zero by maintaining constant specimen and inner cavity volumes (V and V_i), while mechanical and servo-control systems prevented axial straining, allowing only torsional rotation to occur.

Table 4 provides an overview of the 23 undrained cyclic triaxial tests performed on intact Cowden samples from 3.4 m below ground level (bgl.). Reconsolidation was performed to the in-situ stresses with effective stress change rates no faster than 1 kPa/h. All specimens were held under drained conditions at q = -25 kPa and p' = 67 kPa until the axial strain creep rate fell below 0.005%/day. Multiple specimens were cycled directly from these conditions. However, larger numbers were cycled from higher mean q_m values and these were loaded, undrained, to the desired (pre-cycling) q_m values, adopting axial stress change rates of 2 kPa/h rates on most cases. The specimens were then kept undrained until their axial creep rates became negligible (<0.005%/day). Regular undrained sinusoidal cyclic deviatoric stress cycles were then applied with periods (in most cases) of 5 min (0.0033 Hz) per cycle. Cyclic failure was defined as occurring when either: i) the axial strains, of either sign, exceeded 10%, or ii) the strain rates became too high for the actuators to maintain the required stress paths. Ushev (2018) assessed the impact of varying loading rates under monotonic conditions and confirmed that a 10-fold increase in strain rate could result in a 6% increase in undrained shear strengths and 10-14% gain in non-linear stiffnesses. Further details are found in Ushev and Jardine (2020a).

Table 3. Summary of the undrained HCA test conditions

Depth (m)	Test name †	e_o*	σ_{v0}' (kPa)	σ_{h0}' (kPa)	α_f (o)	b_0
2.93	CA0005	0.461	38.7	58.1	0	0.5
2.93	CA2305	0.428	38.7	58.1	23	0.5
2.87	CA6705	0.463	38.0	56.9	67	0.5
2.93	CA9005	0.463	38.7	58.1	90	0.5
2.93	CASS	0.460	38.7	58.1	48.2	1.0
2.87	CATC1	0.471	38.0	56.9	0	1.0
2.87	CATC2	0.441	38.0	56.9	0	1.0
0.5	CTSS	0.573	14.5	21.8	46.7	1.0

† CA0005-CA9005: constant $\alpha_{d\sigma}$ tests; CASS, CTSS: hollow cylinder simple shear tests; CATC1, CATC2: hollow cylinder triaxial compression tests; full details see Liu (2018). * void ratio after consolidation and creep stages and prior to probing.

Table 4. Overview of the undrained cyclic triaxial tests on intact Cowden samples from 3.4 mbgl

Number of tests	q_m (kPa)	q_{cyc} (kPa)	p_0' (kPa)	Final e
11	-25	10~150	64.4~93.1	0.411~0.442
6	50	10~150	65.3~91.5	0.406~0.451
5	125	10~100	93.1~104.8	0.411~0.468
1	200	10	170.6	0.427

4. Anisotropic stiffness and shear strength characteristics

4.1. Linear elastic cross-anisotropic stiffness framework

Treating the till's initial linear elastic behaviour as being cross-anisotropic and strain-rate independent allowed moduli from dynamic and static procedures to be considered as compatible and inter-comparable. Following the approaches set out by Gasparre et al. (2007) and Nishimura (2014), the cross-anisotropic linear elastic stiffness can be characterised by five independent parameters, E_v', E_h', ν_{hv}' (or ν_{vh}'), G_{vh}, G_{hh} (or ν_{hh}'). Under undrained conditions, the number of independent parameters further reduces to three (E_v^u, E_h^u,

G_{vh}). Shear moduli in the vertical (G_{vh} and G_{hv}) and horizontal (G_{hh}) planes can be measured non-destructively by bender elements. The undrained vertical and horizontal Young's moduli can be interpreted with a drained approach (see for example Brosse et al. (2016)) through the following equations.

$$E_v^u = \frac{E_v'[2(1-\nu_{hh}')E_v' + (1-4\nu_{vh}')E_h']}{2(1-\nu_{hh}')E_v' - 4(\nu_{vh}')^2 E_h'} \quad (1)$$

$$E_h^u = \frac{E_h'[2(1-\nu_{hh}')(E_v')^2 + (1-4\nu_{vh}')E_v'E_h']}{[1-(\nu_{hh}')^2](E_v')^2 + (1-2\nu_{vh}' - 2\nu_{vh}'\nu_{hh}')E_v'E_h' - (\nu_{vh}')^2(E_h')^2} \quad (2)$$

Recognising the difficulty of measuring radial strains reliably, Nishimura (2014) proposed a combined drained and undrained probing approach that relies only on the generally higher quality axial strain data. The approach requires additional undrained vertical probes to determine the undrained vertical Young's modulus, E_v^u and the drained horizontal Young's modulus, E_h' can be derived through the following equation.

$$E_h' = \frac{4G_{hh}(E_v^u - E_v')}{E_v^u + 4a^2E_v^uE_v'G_{hh} + (1-4aE_v')G_{hh} - E_v'} \quad (3)$$

where $a = \nu_{hv}'/E_h' = -\Delta\varepsilon_v/(2\Delta\sigma_h')$.

Assuming cross-anisotropic conditions, the r-θ plane in HCA tests is equivalent to the horizontal plane in triaxial tests, except that $E_h = E_r = E_\theta$ and $\nu_{hh} = \nu_{r\theta} = \nu_{\theta r}$. Brosse (2012) proposed the following equations to determine the undrained Young's moduli in the vertical and horizontal planes and the torsional shear stiffness directly over the full strain range $\alpha_{d\sigma}$ tests.

$$E_v^u = \frac{2\Delta\sigma_z - \Delta\sigma_r - \Delta\sigma_\theta}{2\Delta\varepsilon_z} \quad (4)$$

$$E_{hr}^u = \frac{\Delta\sigma_r(\Delta\sigma_r - 2\Delta\sigma_z) - \Delta\sigma_\theta(\Delta\sigma_\theta - 2\Delta\sigma_z)}{\Delta\varepsilon_r(\Delta\sigma_r + \Delta\sigma_\theta - 2\Delta\sigma_z) + \Delta\varepsilon_z(\Delta\sigma_\theta - \Delta\sigma_z)} \quad (5)$$

$$E_{h\theta}^u = \frac{\Delta\sigma_r(\Delta\sigma_r - 2\Delta\sigma_z) - \Delta\sigma_\theta(\Delta\sigma_\theta - 2\Delta\sigma_z)}{\Delta\varepsilon_\theta(\Delta\sigma_r + \Delta\sigma_\theta - 2\Delta\sigma_z) + \Delta\varepsilon_z(\Delta\sigma_r - \Delta\sigma_z)} \quad (6)$$

$$G_{z\theta} = \frac{\Delta\tau_{z\theta}}{\Delta\gamma_{z\theta}} \quad (7)$$

4.2. Anisotropic small- and large-strain stiffness characteristics

Examples of stress-strain loops recorded in the small-strain probing tests are plotted in Fig. 2-3, covering the vertical ($+\Delta\sigma_v'$, $-\Delta\sigma_v'$) and horizontal ($+\Delta\sigma_h'$, $-\Delta\sigma_h'$) probes in test PB2. Given the very small strains considered, the individual data points inevitably show scatter. However, the cycles appear fully reversible and the probes gave similar linear slopes, regardless of the sign or size of the load increment over the ranges considered. Liu et al. (2020) reported the full details of the drained and undrained cross-anisotropic compliance parameters derived from the triaxial probing and bender element measurements, applying the approaches set out in Eqs (1-3). The results indicated that Cowden till manifests anisotropy with elastic moduli that are stiffer under horizontal than vertical loading, with in most cases $G_{hh} > G_{vh}$, $E_h' > E_v'$ and $E_h^u > E_v^u$. The anisotropy ratios, G_{hh}/G_{vh}, E_h'/E_v' and E_h^u/E_v^u, derived from the triaxial probing and HCA tests are plotted against depth in Fig. 4, where they show generally consistent trends. Also shown are the shear modulus ratios (G_{hh}/G_{vh} and G_{hh}/G_{hv}) determined from in-situ down-hole and cross-hole shear velocity tests reported by Powell & Butcher (2003). In general, the till's stiffness anisotropy is most prominent in shallow depths but appeared to diminish with depth.

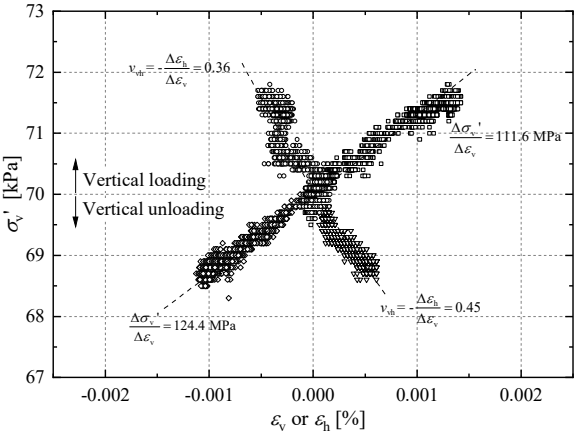

Figure 2. Stress-strain increments in the drained vertical loading (+dv′) and unloading (-dv′) probes in test PB2.

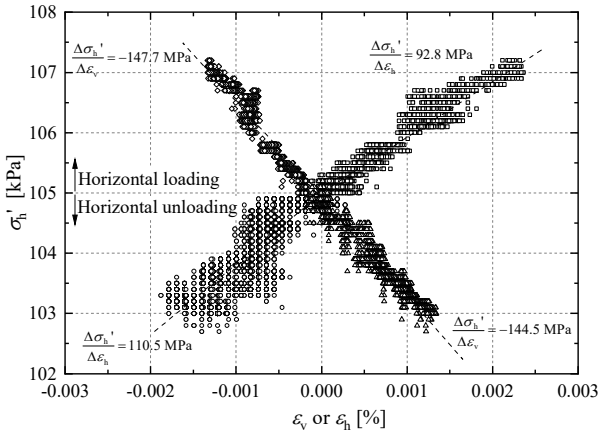

Figure 3. Stress-strain increments in the drained horizontal loading (+dh′) and unloading (-dh′) probes in test PB2.

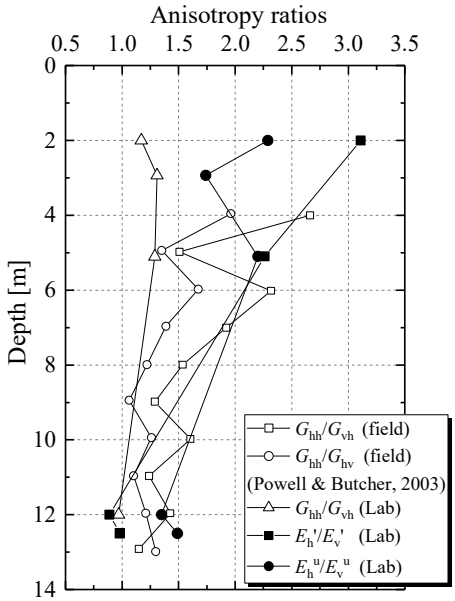

Figure 4. Anisotropic stiffness profile of the Cowden till site.

The till's marked elastic-plastic stiffness degradation with strain under HCA conditions is demonstrated in

Figs. 5-6 by plotting E_v^u and E_h^u against vertical strain ε_z and average horizontal strain $(\varepsilon_r + \varepsilon_\theta)/2$, respectively. Despite scattering over the tests' initial sections, the undrained Young's moduli exhibited consistent degradation trends. Narrow spreads were observed for each component, suggesting that the cross-anisotropic stiffness components are relatively insensitive to the shearing path followed, even over the non-linear range. The two HCA triaxial tests (CATC and CATC2), which employed $b = 1.0$, showed encouraging overlapping E_v^u trends that fall slightly below those of most $b = 0.5$ tests. Overall, the E_h^u curves plot above the E_v^u data trends, confirming that stiffness anisotropy persists beyond the till's linear elastic ranges.

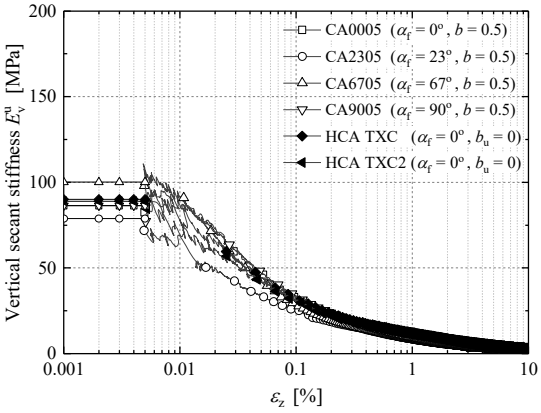

Figure 5. Degradation of undrained vertical Young's Moduli E_v^u against vertical (axial) strain.

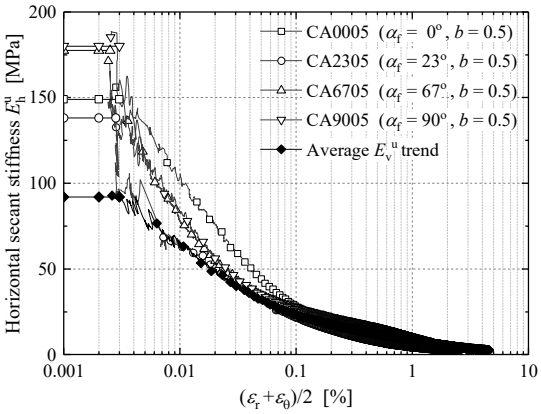

Figure 6. Degradation of undrained horizontal Young's Moduli E_h^u against horizontal strain.

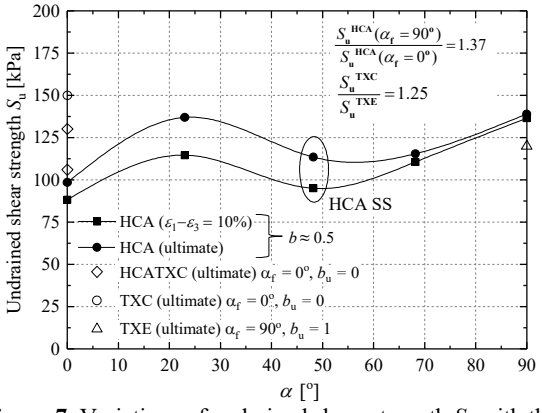

Figure 7. Variations of undrained shear strength S_u with the orientation of major principal stress.

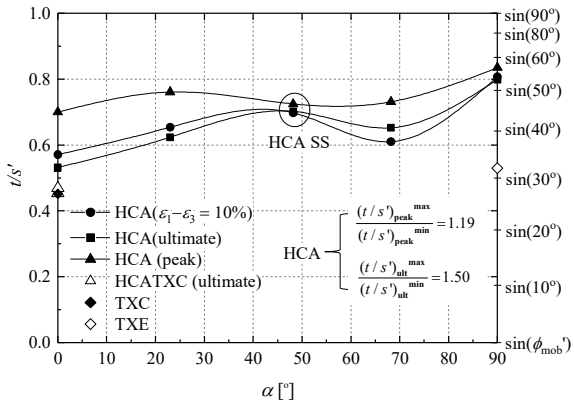

Figure 8. Variations in stress ratio t/s' with the orientation of major principal stress.

4.3. Undrained shear strength anisotropy

The shear strengths were considered in terms of Tresca undrained shear strengths S_u (= $q/2$) and secant Mohr Coulomb stress ratios t/s' (taking $c' = 0$). Under nominally plane strain conditions with $b = (\sigma_2 - \sigma_3)/(\sigma_1 - \sigma_3) = 0.5$, the passive test (CA9005) with $\alpha_f = 90^\circ$ showed the highest undrained shear strength ($S_u = q_{max}/2$), while the sample that underwent active compression failure (CA0005) with $\alpha_f = 0^\circ$ exhibited the lowest; simple shear failure was achieved with $b \approx 0.5$ and $\alpha_f \approx 48^\circ$. The undrained shear strengths of the specimens experiencing mainly torsional shearing at intermediate α_f values spanned these limits. Fig. 7 shows the variations of S_u with the orientation of major principal stress, noting that the highest shear strength is developed under nominally plane strain compression conditions ($\alpha_f = 90^\circ$) and the lowest at $\alpha_f = 0^\circ$, under active plane strain stresses. The till's anisotropic shear strength characteristics are also summarised in terms of stress ratio t/s' at 10% shear strain, peak and ultimate states, as shown in Fig. 8. As with the Tresca criterion, the minimum t/s' develops at $\alpha_f = 0^\circ$, and the maximum at $\alpha_f = 90^\circ$. A ratio of 1.19 exists between the maximum and minimum, with the highest value corresponding to remarkably high secant ϕ_{mob}' angle.

5. Undrained cyclic triaxial loading behaviour

5.1. Number of cycles to failure and cyclic interaction diagrams

The interactive influences of the mean q_m and cyclic q_{cyc} deviatoric stresses outlined in Table 4 were explored in the normalised stress space shown in Fig. 9. Two parallel schemes for normalising were employed, including the conventional total stress $q_{cyc}/2S_u$ and $q_m/2S_u$ measures and an alternative 'effective-stress' normalised axes with $q_{cyc}/p'_{in\text{-}situ}$ and $q_m/p'_{in\text{-}situ}$. Five of the higher amplitude cyclic tests failed according to the adopted criteria after the indicated number (N_f) of cycles. All other specimens remained un-failed when the loading halted after 1500 to 3500 cycles. Interpreted contours are shown in Fig. 9 of the cyclic stress combinations under which the tests indicated failure after $N = 10$, 100 or 1000 cycles. The contours were established by semi-logarithmic interpolation between the experimental

results. The failed tests' N_f values are also annotated; points marked with a '>' sign represent cases that remained un-failed at the specified total number of cycles. The interaction diagram may be separated into an un-failed zone and regions where failures occurred by either (i) a combination of large cyclic and average strains, that led to "abrupt failure" or (ii) cases where large mean strains developed without correspondingly large cyclic strains and samples failed through "creep".

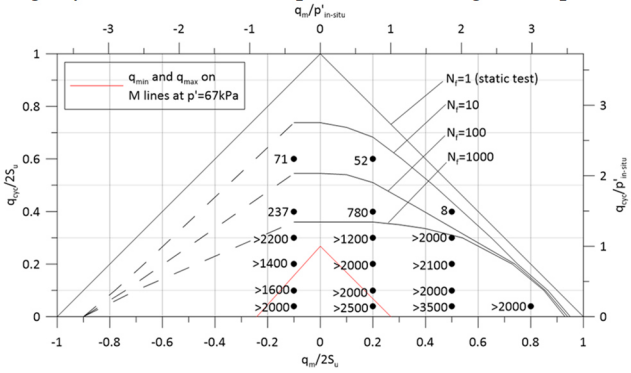

Figure 9. Contours of number of cycles to failure in stress space nomalised by undrained shear strength (S_u) and in-situ mean effective stress ($p'_{in-situ}$).

5.2. Evolution of effective stress, cyclic strain and stiffness

The cycle-by-cycle effective stress paths, which were tracked accurately throughout, varied systematically with the loading parameters ($q_m/(2S_u)$, $q_{cyc}/(2S_u)$ or $q_{cyc}/p'_{in-situ}$ and $q_m/p'_{in-situ}$) and N. Typical outcomes of 'stable' and 'unstable' cyclic response are presented in Figs. 10-11 for a set of experiments cycled under relatively low q_{cyc} of 25 kPa and a single test subjected to the highest amplitude of cycling with q_{cyc} = 150 kPa from 'in-situ' q_m = -25 kPa. Also shown in these plots are the no-tension lines, the Hvorslev surfaces and failure M lines identified from the static tests. As shown in Fig. 10, the experiments involving q_{cyc} = 25 kPa ($q_{cyc}/2S_u$ = 0.1) amplitude exhibited broadly stable responses. Shifts can be seen from an initially "dilative" drift trend to one indicating slightly "contractive" behaviour. The tests' overall $|\Delta p'/p'_0|$ changes were smaller than 5% over the 1697 to 2013 cycles applied in the q_m = -25 kPa cases, while the q_m =125 kPa test, which also approached the Hvorslev surface showed a 6% drift.

The higher amplitude q_{cyc} = 100 and 150 kPa ($q_{cyc}/2S_u$ = 0.4 and 0.6) experiments conducted from q_m = -25, 50 and 125 kPa all first violated the 'slow shearing' Hvorslev surface and subsequently progressed to fail within 1000 cycles, as illustrated in Fig. 11. Their final stages involved cyclic axial strain rates of 10 to more than 1000%/h, which were up to 200 times higher than in the reference monotonic experiments, which may explain again why they were able to occupy regions of effective stress space that were inadmissible in the slower tests. Their initial cyclic effective stress paths showed markedly dilative behaviour, which the till could not sustain for many cycles. The specimens' p′ values started to fall more significantly on unloading than they rose during loading, leading to a contractive overall trend with the paths heading leftward towards the origin, developing irregular loops and broad "butterfly" shapes.

Typical patterns of permanent axial strain (ε_{mean}) accumulation with number of cycles (N) are demonstrated in Fig. 12. employing logarithmic axes and showing the experiments cycled from q_m = -25 kPa.

All the experiments developed some permanent straining, although three of the four tests that sustained the lowest (10 kPa) cyclic amplitudes tended to stabilise after 100 to 1000 cycles and had rates that were often comparable to the slow residual creep rates (<0.005%/day) applying before cyclic started. Ushev (2018) found the broad trends seen over the full durations of all tests that manifested stable or metastable effective stress paths, and those from the initial stages of unstable tests, appear to follow approximately power law relationships with N. Empirical relationships were proposed to link the power-law coefficients with the cyclic loading q_{cyc} and q_m parameters.

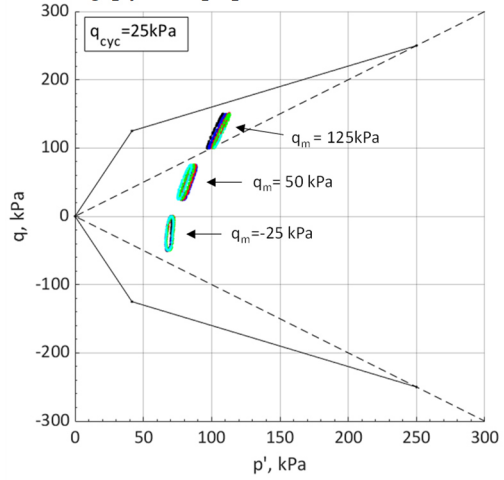

Figure 10. Cyclic effective stress paths with q_{cyc} = 25 kPa.

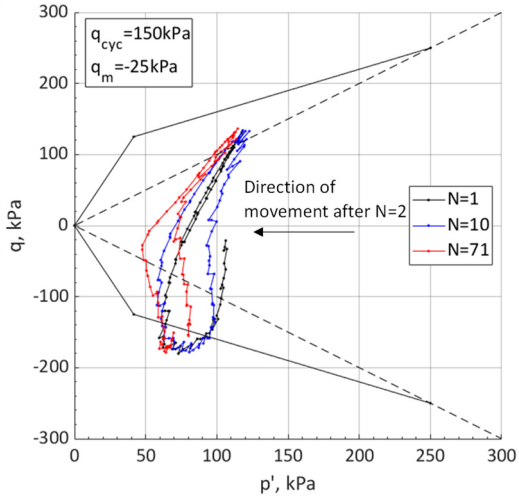

Figure 11. Effective stress paths during cycling with q_{cyc} = 150 kPa and q_m = -25 kPa.

Ushev (2018) noted four alternative $\Delta q/\Delta\varepsilon$ combinations may be adopted to derive undrained cyclic secant vertical equivalent Young's Moduli (E_u^{sec}) and considered the average from the four possible combinations to be the most representative measure. One of the resulting trends for the average cyclic secant stiffness is presented in Fig. 13 for tests performed at in-situ q_m. The tests that manifested stable effective stress

loops (and remained within the till's Y_2 kinematic yield surfaces) showed stiffness either growing slightly with N or falling modestly before stabilising. Cycling within the Y_2 kinematic yield surface (at constant overall volume and with little change in p') generates repetitive plastic shear strains that appear to stiffen the soil's response under the applied loading.

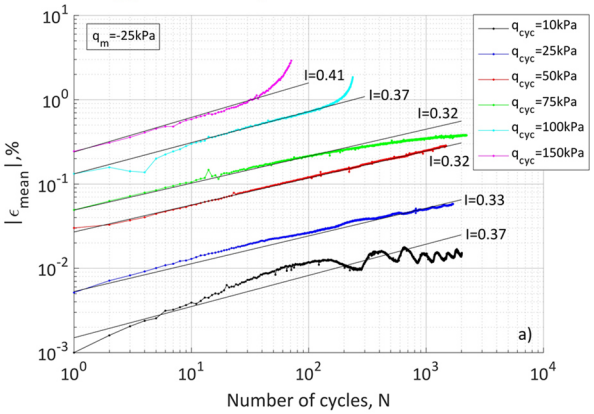

Figure 12. Variation of mean (permanent) axial strain with number of cycles for tests cycled from q_m = -25 kPa.

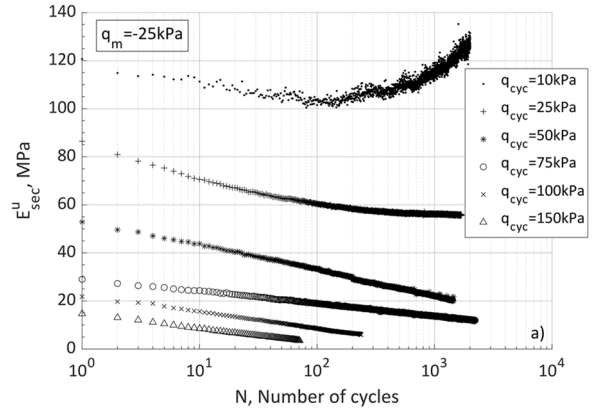

Figure 13. Cyclic secant stiffness against number of cycles at q_m = -25 kPa.

5.3. Cyclic kinematic yield surfaces

The cyclic responses observed in stable and metastable tests can be related to two kinematic yield surfaces that, once engaged, move with the current effective stress point. Ushev (2018) showed from monotonic stress probing tests that the first elastic, Y_1, region is approximately elliptical in shape and has a maximum height of only about ±2.5 kPa in-situ at the 3.0 to 3.5m cyclic series' sampling depth. The second Y_2 kinematic yield surface (KYS) was defined as the threshold limit to: (i) stable effective stress conditions that involve less than 5% variation in p' over 2000 ±500 cycles and (ii) practically constant cyclic stiffness. The experiments showed that tests that satisfy these two criteria also tended to exhibit low damping ratios and energy dissipation per cycle, as well as low and stabilising axial strain rate trends. Fig. 14 marks the approximate boundaries of the Y_1 (red circles) and Y_2 (black ellipses) kinematic yield surfaces that surround each q_m point, along with the points at which large scale (Y_3) yielding developed under cyclic loading, which are shown as squares. The Y_2 surfaces' vertical dimensions were seen to diminish as the pre-loading effective conditions approached the outer Hvorslev boundary, even though p' increased as the samples moved along this undrained loading path. While cyclic loading within the initial Y_2 kinematic yield surface does not appear deleterious, paths that engage Y_2 on each loading and unloading stages dissipate far more energy and provoke marked stiffness degradation and strain accumulation.

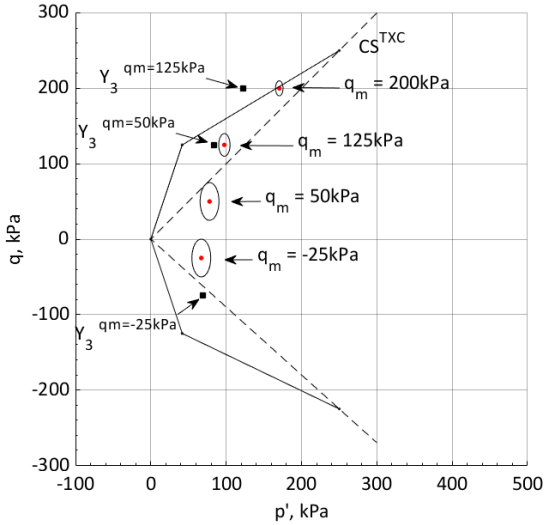

Figure 14. Y_2 Kinematic Yield Surfaces and Y_3 cyclic yield points interpreted from cyclic undrained tests. Note 'linear elastic' Y_1 surfaces indicated by red dots have vertical extents of approximately ±2.5 kPa.

6. Conclusions

Accurate geotechnical characterisation of high YSR, stiff glacial tills is critical for a range of onshore and offshore design problems. This paper reports on coordinated monotonic small-strain stress probing, cyclic and larger strain triaxial and hollow cylinder apparatus (HCA) experiments that investigated the mechanical anisotropy and undrained cyclic loading behaviour of a Bolders Bank Formation glacial till sampled at Cowden (NE England). The key findings are:

(1) The till manifested fully recoverable and linear elastic stiffness over only a very small strain range. This behaviour was markedly anisotropic, with far higher drained and undrained stiffnesses under horizontal than vertical loading and G_{hh0}/G_{vh0}, E_{h0}'/E_{v0}', E_{h0}^u/E_{v0}^u greater than unity. The stiffness anisotropy persisted over the non-linear range.

(2) The till also manifested shear strength anisotropy, following a pattern that differed considerably from the patterns expected with low *OCR* sediments. The minimum strengths developed at α = 0° vertical compression and the maximum at α = 90° lateral compression, with the torsional shear mode ($\alpha_f \approx$ 45°) strengths in between.

(3) The cyclic test outcomes, which could be summarised succinctly in contoured interaction diagrams, established the influences of the cyclic loading parameters on the number of cycles to failure, mean effective stress drifts, accumulated (mean) and cyclic (amplitude) strains.

(4) The till's cyclic behaviour remained linear elastic within an initial Y_1 kinematic yield surface applying over a very limited range of q-p' stress space. Y_2

kinematic yield surfaces were also identified from the cyclic tests that set the cyclic effective stress space within which completely stable cyclic response may be expected with negligible mean effective stress drifts and stiffness degradation.

Acknowledgements

The Cowden sampling was undertaken by Concept Drilling Service Ltd and Socotec, as part of the PISA JIP project managed by Ørsted. The PISA sponsors' and Academic Working Group's support is acknowledged, as is the financial support from the PISA JIP and Orsted (through a Post-PISA project). The Imperial College technicians, Steven Ackerley, Graham Keefe, Alan Bolsher and Duncan Parker are thanked for enabling the taxing experimental work. The kind support and helpful discussion offered by Professors Satoshi Nishimura (Hokkaido University) and Stavroula Kontoe (University of Patras) and Drs Amandine Brosse (GCG) and Amin Aghakouchak (Ørsted) is also acknowledged gratefully.

References

Addenbrooke, T. I., D. M. Potts, A. M. Puzrin "The influence of pre-failure soil stiffness on the numerical analysis of tunnel construction" Géotechnique, 47(3), 693-712, 1997. https://doi.org/10.1680/geot.1997.47.3.693

Andersen, K. "Bearing capacity under cyclic loading - Offshore, along the coast, and on land". Canadian Geotechnical Journal, 46 (5), 513–535, 2009. https://doi.org/10.1139/T09-003

Andersen, K. "Cyclic soil parameters for offshore foundation design". Meyer (ed.). Frontiers in Offshore Geotechnics III, ISFOG.1 pp.5-82, 2015.

Brosse, A. M., R. Hosseini Kamal, R. J. Jardine, M. R. Coop. "The shear stiffness characteristics of four Eocene-to-Jurassic UK stiff clays". Géotechnique, 67(3), 242-259. 2017, https://doi.org/10.1680/jgeot.15.P.236

Brosse, A. M., R. J. Jardine, S. Nishimura. "The undrained shear strength anisotropy of four Jurassic to Eocene stiff clays" Géotechnique, 67(8), 653-671, 2017. https://doi.org/10.1680/jgeot.15.P.227

Byrne, B. W., R. A. McAdam, H. J. Burd, G. T. Houlsby, C. M. Martin, W. Beuckelaers, L. Zdravkovic, D. M. G. Taborda, D. M. Potts, R. J. Jardine, E. Ushev, T. Liu, D. Abadias, K. Gavin, D. Igoe, P. Doherty, J. S. Gretlund, M. P. Andrade, A. Muir Wood, F. Schroeder, S. Turner, M. Plummer. "PISA: New design methods for offshore wind turbine monopiles". Society for Underwater Technology: 8th International Conference on Offshore Site Investigation and Geotechnics, London, UK, vol. 1, pp. 142-161, 2017.

Byrne, B. W. "Lateral pile design for offshore wind turbines" In Piling 2020: Proceedings of the Piling 2020 Conference, pp. 13-33. ICE Publishing, 2021.

Clarke, B. G., D. B. Hughes, S. Hashemi. Physical characteristics of subglacial tills. Géotechnique, 58(1), 67-76, 2018. https://doi.org/10.1680/geot.2008.58.1.67

Clarke, B. G. "The engineering properties of glacial tills". Geotechnical Research 5(4), 262-277, 2018. https://doi.org/10.1680/jgere.18.00020

Davies, B. J., D. H. Roberts, D. R. Bridgland, C. Ó Cofaigh, J. B. Riding. "Provenance and depositional environments of Quaternary sediments from the western North Sea Basin" Journal of Quaternary Science. 26(1), 59-75, 2011. https://doi.org/10.1002/jqs.1426

Fullerton, D. S., C. A. Bush, J. N. Pennell. Map of surficial deposits and materials in the eastern and central United States (East of 102 degrees West longitude. Report 2789, 2003. https://doi.org/10.3133/i2789

Gasparre, A., S. Nishimura, N. A. Minh, M. R. Coop, R. J. Jardine. 2007 "The stiffness of natural London Clay". Géotechnique, 57(1), 33-47. https://doi.org/10.1680/geot.2007.57.1.33

Jardine, R. J., K. Andersen, A. Puech. "Cyclic loading of offshore piles: potential effects and practical design". Proc 7th Int. Conf. on Offshore Site Investigations and Geotechnics, SUT London, pp 59-100, 2012.

Jeanjean, P., Y. Zhang, A. Zakeri, K. Andersen, R. Gilbert, A. I. M. J. Senanayake. "A framework for monotonic p-y curves in clays". Society for Underwater Technology: 8th International Conference on Offshore Site Investigation and Geotechnics, London, UK, vol. 1, pp. 108-141, 2017.

Liu, T. "Advanced laboratory testing for offshore pile foundations under monotonic and cyclic loading", PhD Thesis, Imperial College London, 2018.

Liu, T., E. Ushev, R. J. Jardine. "Anisotropic stiffness and shear strength characteristics of a stiff glacial till". ASCE J. of Geotech. Geoenv. Eng., 146(12), 2020 https://doi.org/10.1061/(ASCE)GT.1943-5606.0002387

Liu, T., R. J. Jardine, K. Vinck, S. K. Ackerley. "Optimization of advanced laboratory monotonic and cyclic triaxial testing on fine sands". ASTM Geotechnical Testing Journal 45(6), 2022. https://doi.org/10.1520/GTJ20210190

Nishimura, S., N. A. Minh, R. J. Jardine. "Shear strength anisotropy of natural London Clay". Géotechnique, 57(1), 49-62, 2007. https://doi.org/10.1680/geot.2007.57.1.49

Nishimura, S. "Cross-anisotropic deformation characteristics of natural sedimentary clays". Géotechnique 64(12):981-996, 2014. https://doi.org/10.1680/geot.14.P.088

Powell, J., A. Butcher. "Characterisation of a glacial clay till at Cowden, Humberside". In Proceedings of the Int. Workshop on Characterisation and Engineering Properties of Natural Soils. (Tan, T. S., Phoon, K. K., Hight, D. W. & Leroueil, S. (Eds)) CRC Press, London, 983-1020, 2003.

Ratananikom, W., S. Likitlersuang, S. Yimsiri. "An investigation of anisotropic elastic parameters of Bangkok Clay from vertical and horizontal cut specimens". Geomechanics and Geoengineering 8(1), 15-27, 2013. https://doi.org/10.1080/17486025.2012.726746

Ushev, E. "Laboratory investigation of the mechanical properties of Cowden till under static and cyclic conditions", PhD Thesis, Imperial College London, 2018.

Ushev, E., R. J. Jardine. "The behaviour of Bolders Bank glacial till under undrained cyclic loading". Géotechnique, 72(1), 1-19, 2022a. https://doi.org/10.1680/jgeot.18.P.236

Ushev, E., R. J. Jardine. "The mechanical behaviour of Bolders Bank till". Canadian Geotechnical Journal, 59, 2163-2183, 2022b. https://doi.org/10.1139/cgj-2021-0436

Ushev, E., T. Liu, R. J. Jardine. "Engineering properties of a stiff Bolder Bank glacial till at Cowden". Submitted to Offshore Site Investigation and Geotechnics Conference, Society of Underwater Technology, London, UK, 2023.

Wichtmann, T., A. Niemunis, T. Triantafyllidis. "Strain accumulation in sand due to cyclic loading: drained triaxial tests". Soil Dyn. and Earthquake Eng., 25 (11), 967–979, 2005. https://doi.org/10.1016/j.soildyn.2005.02.022

Zdravković, L., D. M. Potts, R. J. Jardine (2001). A parametric study of the pull-out capacity of bucket foundations in soft clay. Géotechnique, 51, 1 pp 55 -67. https://doi.org/10.1680/geot.2001.51.1.55

Zdravković, L., B. W. Byrne, D. M. G. Taborda, H. J. Burd, K. Gavin, G. T. Houlsby, D. Igoe, R. J. Jardine, T. Liu, C. M. Martin, R. A. McAdam, A. Muir Wood, D. M. Potts, J. Skov Gretlund, E. Ushev "Ground characterisation for PISA pile testing and analysis". Géotechnique, 70(11), 945-960, 2020. https://doi.org/10.1680/jgeot.18.PISA.001